**Supplementary Information**

# Engineering Ultra-small $CeO_2$ NPs with Antioxidant and UV-shielding Properties as Functional Nanomaterials in Composite Coatings for Complex Surface Protection

*Erica Galvagno, Sergio Marras, Silvia Dante, Rosaria Brescia, Miquel Gamón Rodríguez, Alessio Carmignani, Matteo Battaglini, Gianni Ciofani, Raffaella Lamuraglia, Federica Menegazzo, Arianna Traviglia*, and Mauro Moglianetti**

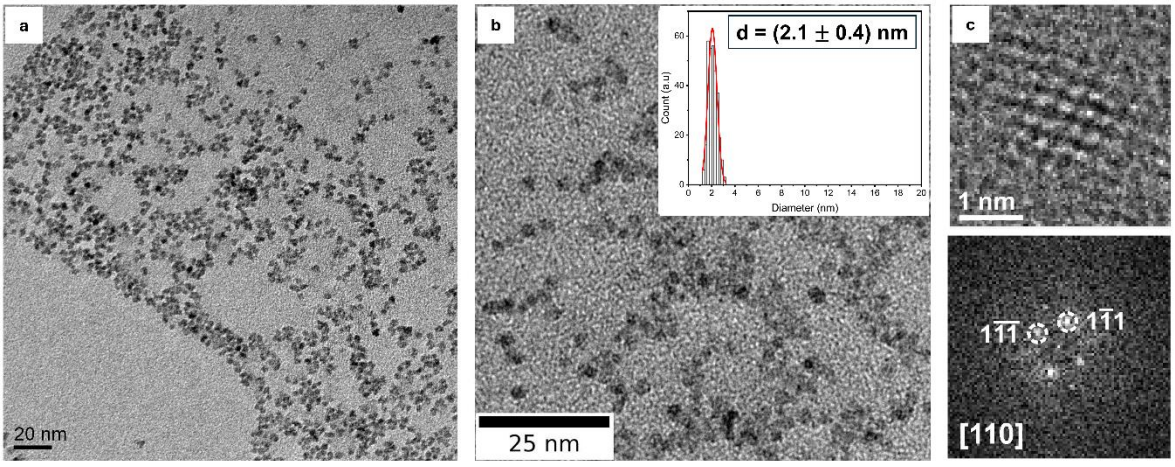


**Figure S1. a,** BF-TEM image of a-NPs. **b,** BF-TEM image of t-NPs with the corresponding size distribution (insert). **c,** HRTEM image and corresponding FFT of an individual t-NP, indexed based on cubic $CeO_2$ (ICSD 155604).

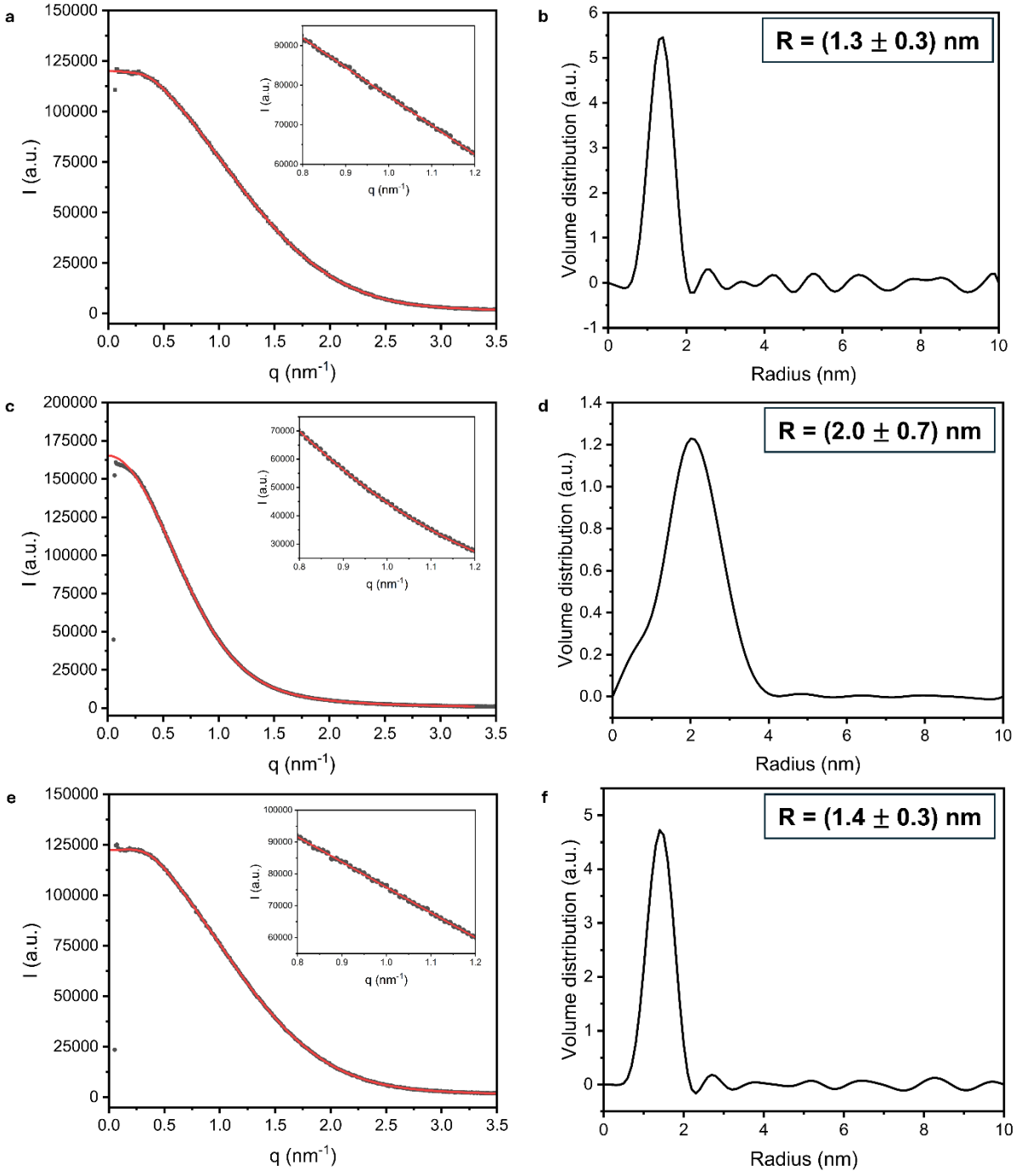


**Figure S2. a,** Experimental curve (black dots) and fit (red line) of SAXS measurements of t-NPs (in the insert: zoomed-in portion of the graph). **b,** Size distribution by volume of t-NPs, obtained from SAXS measurements. **c,e,** Experimental curve (black dots) and fit (red line) of SAXS data of a-NPs (**c**) and t-NPs (**e**) 6 months after the preparation (in the insert: zoomed-in portion of the graph). **d,f,** Size distribution by volume of a-NPs (**d**) and t-NPs (**f**) 6 months after the preparation, obtained from SAXS measurements.

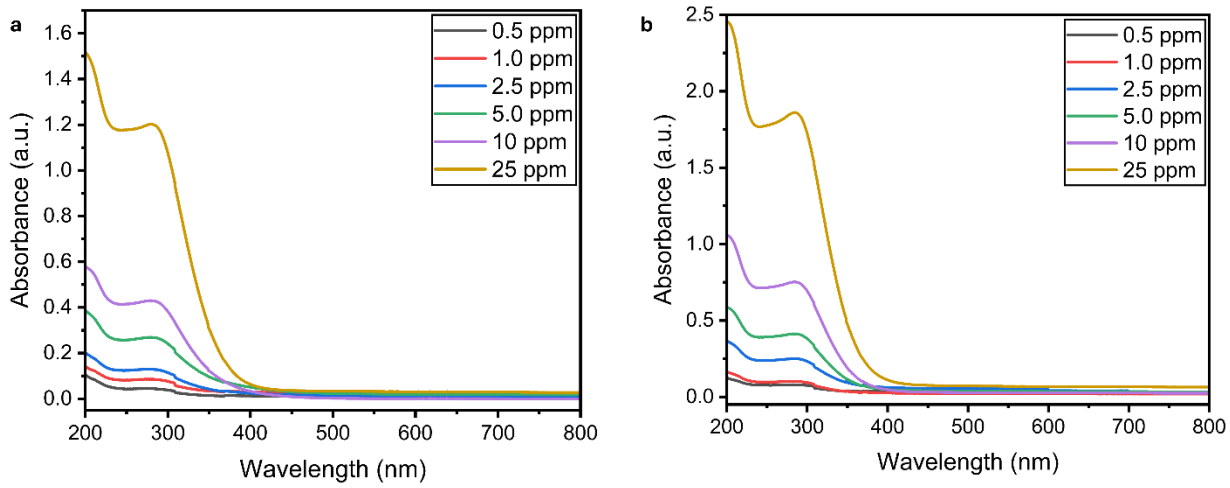


**Figure S3. a,** UV-visible spectrum of a-NPs at different concentrations. **b,** UV-visible spectrum of t-NPs at different concentrations. All concentrations tested in the enzyme-like activity assessment are reported.

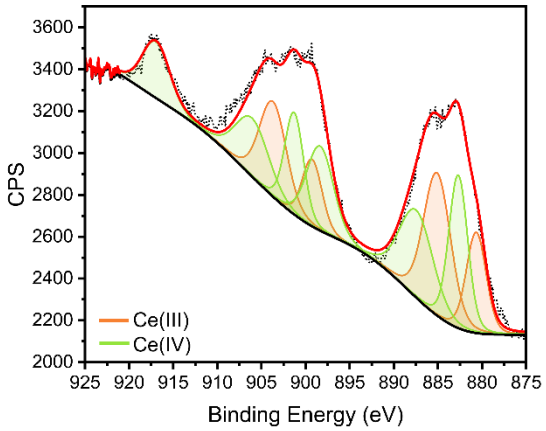


**Figure S4.** Ce 3d region of t-NPs where Ce(III) (orange) and Ce(IV) (green) have been fitted. The measurements were acquired in an Ar atmosphere for the NPs deposited and dried on silicon wafer.

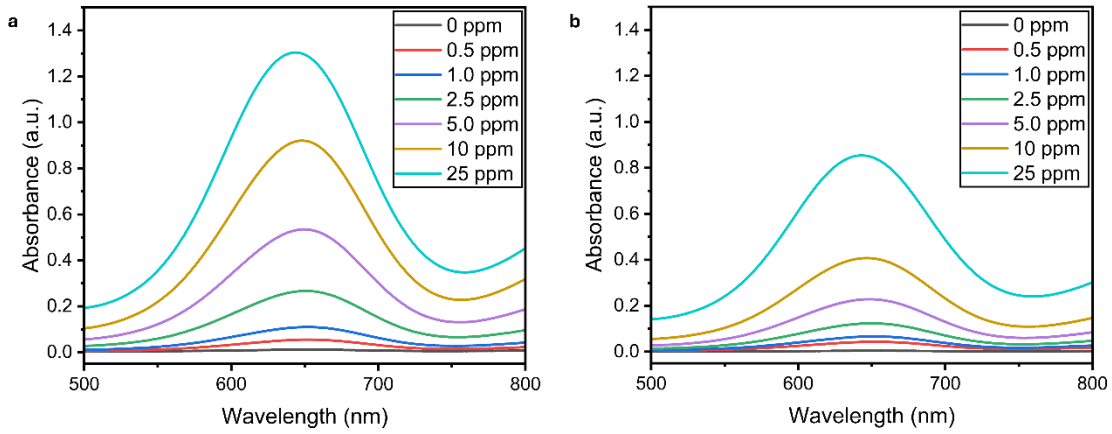


**Figure S5. a,** Peroxidase-like activity of t-NPs determined in an ultrapure water solution by studying its interaction with $H_2O_2$ in the presence of TMB. **b,** Oxidase-like activity of t-NPs determined in an ultrapure water solution by studying its interaction with $O_2$ in the presence of TMB.

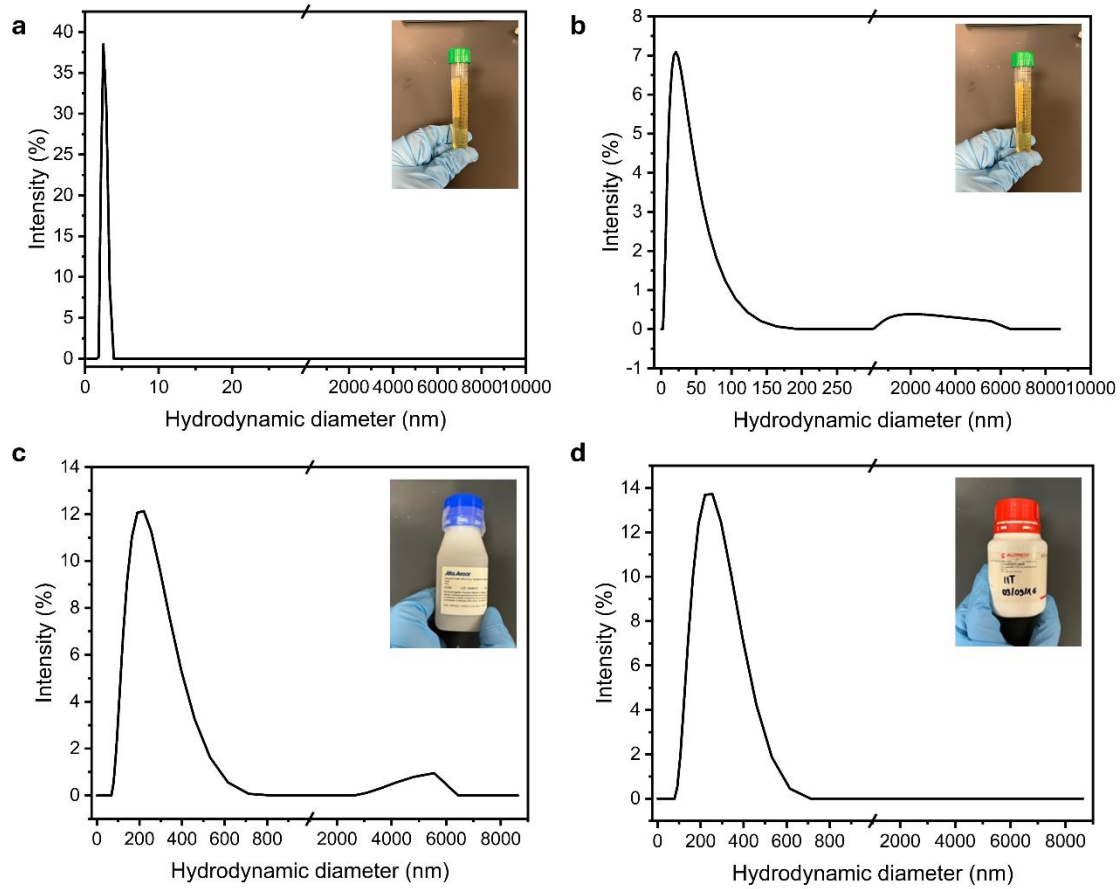


**Figure S6.** Hydrodynamic diameter of the following samples. **a,** a-NPs after the synthesis with citrate capping agents. **b**, a-NPs after protein coating. **c,** c1-NPs after protein coating. **d,** c2-NPs after protein coating.

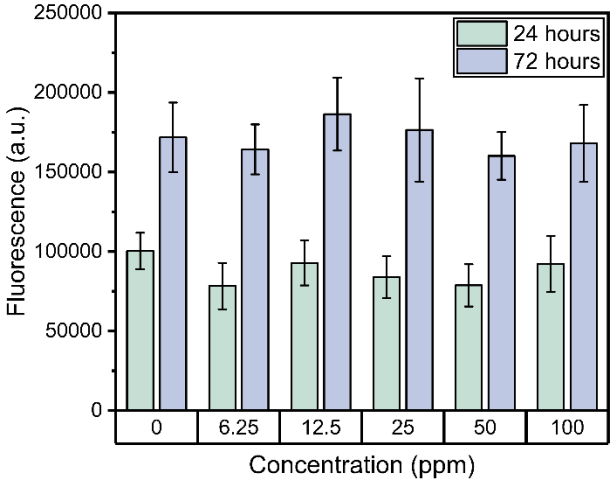


**Figure S7.** PicoGreen assay of t-NPs at two different exposure times, 24 and 72 hours.

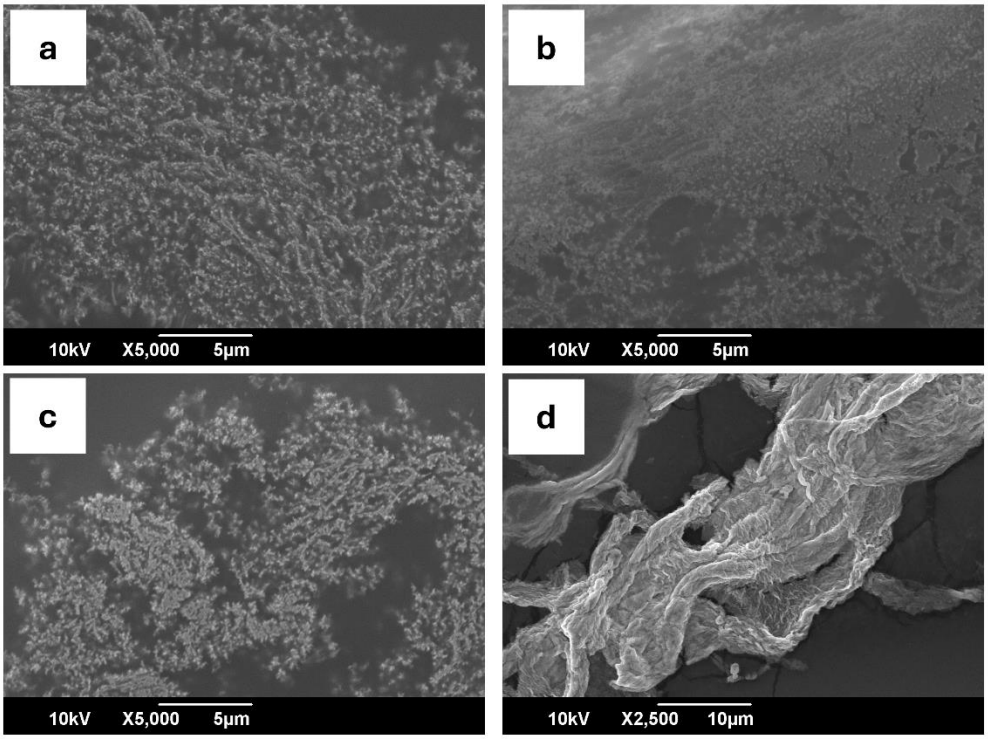


**Figure S8.** SEM images of chitosan formulations: (**a**) cs02; (**b**) cs04; (**c**) cs1; (**d**) cs2.

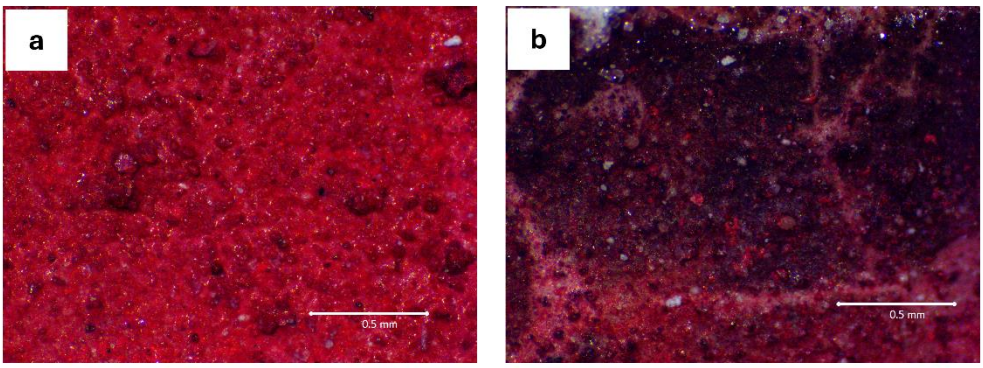


**Figure S9.** Microscope images of cinnabar fresco mock-ups in the following conditions. **a,** Before ageing. **b,** After ageing. Ageing has been achieved through exposure of the sample to UV light, chlorine-based salts and high relative humidity.

Figure S10 schematically represents the mechanisms that have been hypothesized for the degradation of cinnabar (α-HgS). Some works report that the formation of a black compound might indicate the phase transition between cinnabar and metacinnabar (β-HgS) (Eq. 1).[1,2] Nevertheless, this transformation is known to generally happen at high temperatures (315 – 400°C), so this hypothesis has not been univocally accepted.[3] Alternatively, the black color on the surface of degraded cinnabar-painted frescoes could be explained considering the formation of metallic mercury (Hg(0)). On the one hand, environments with high relative humidity might induce a redox mechanism to transform the sulfide ions from cinnabar into sulfate, with the consequent formation of $HgSO_4$ (Eq. 2).[4,5] Taking into account some considerations on the redox potential of $HgSO_4$ and mercury ions, Elert *et al.* state that $HgSO_4$ could be reduced into Hg(0) through a photo-induced electron transfer process (Eq. 3).[4,5] On the other hand, cinnabar could have a photochemical reaction that leads to Hg(0) and S(0) thanks to the catalysis of chloride ions, which have been established to be a critical factor in the degradation of cinnabar (Eq. 4).[6,7] Hg(0) can be responsible for the black color on the surface, but this mechanism could also be followed by other transformations to produce chlorine-based species, showing how interconnected the hypothesized mechanisms can be. Indeed, Hg(0) can potentially react with other chloride ions to produce $HgCl_2$, following Eq. 5.[6,7] Instead, S(0) could interact with atmospheric oxygen to form $SO_2$, which can in turn form gypsum after interacting with $CaCO_3$ from the mortar (Eq. 6 and 7).[8,9] The formation of gypsum and the presence of pollutants in the environment might also lead to the creation of a black crust that might contribute to the darkening effect on frescoes. Lastly, the hypothesis that chlorine-based photosensitive species are formed has been supported by the detection of mercury sulfo-chloride species on altered frescoes. Corderoite (α-$Hg_3S_2Cl_2$) or kenhsuite (γ-$Hg_3S_2Cl_2$) could be formed after cinnabar interacts with chlorine ions, as shown in Eq. 8.[1,3,6,7,10] In particular, the formation of α-$Hg_3S_2Cl_2$ as an intermediate has also been supported by thermodynamic modeling in the

work of Neiman *et al.*.[9] These mercury sulfo-chloride compounds are light-sensitive and can be further converted into calomel ($Hg_2Cl_2$) (Eq. 9 and 10), which is responsible for the clack color observed on the degraded surfaces.[1,7,10] This chlorine-based compound can then undergo photo-induced disproportionation to form Hg(0) and $HgCl_2$ (Eq. 11).[7]

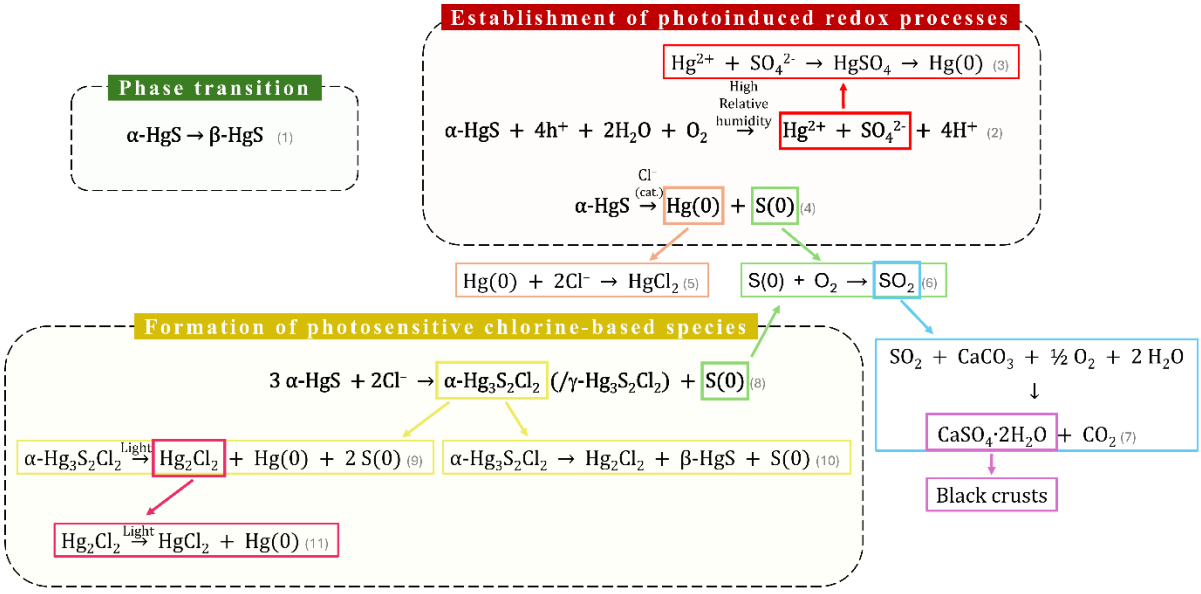


**Figure S10.** Schematic representation of the mechanisms possibly involved in the darkening phenomenon of cinnabar.

The Raman spectrum of cinnabar after degradation suggests the formation of metacinnabar. In Figure S11a, we reported the spectra of cinnabar and of the darkened portions, identified as metacinnabar; the RUFF references for both compounds are reported in Figure S11b.[11,12] The peak determined in the experimental analysis, which is not present in the reference, corresponds to $CaCO_3$ from the mortar beneath the pigment. In the XPS spectra, we identified the same characteristic signals of cinnabar that are reported in the literature.[5,13] In the mercury region of the unaltered sample, Hg $4f_{7/2}$ and Hg $4f_{5/2}$ were identified at 100.5 eV and 104.5 eV, respectively. However, the same peaks have been found in the spectrum of degraded cinnabar, so it is not possible to confirm the formation of Hg(0) (Figure S12a and S12c). For what concerns the region related to sulfur, we identified both sulfide ions from cinnabar and a sulphate species (Figure S12b and S12d). Sulfide ions present a doublet consisting of the S $2p_{3/2}$ component at 161.5 eV and the S $2p_{3/2}$ at 162.7 eV, while sulphate can be identified by the presence of the same doublet at 168.9 eV and 170.1 eV. These two species have been identified both in the unaltered and degraded mock-ups, so sulphate was not entirely formed during the degradation of cinnabar and the observation cannot be used to confirm the establishment of a redox mechanism.

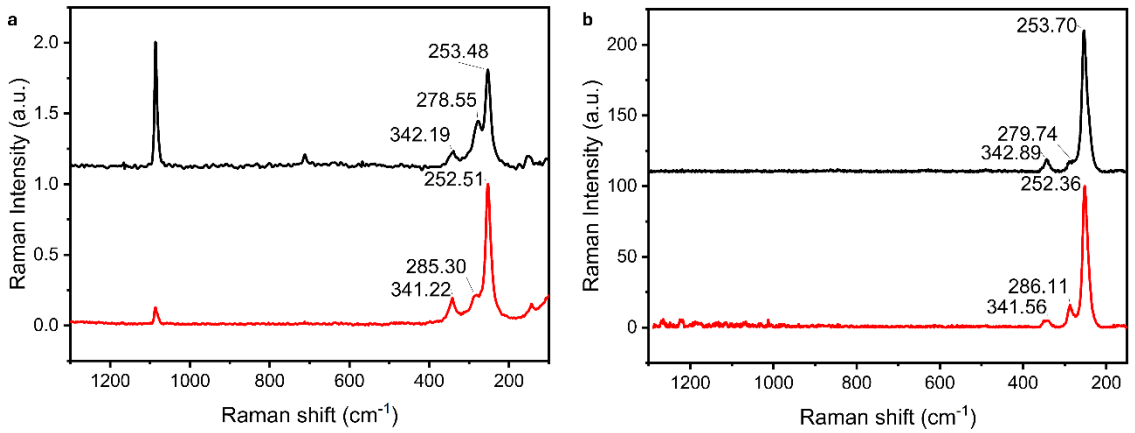


**Figure S11. a,** Raman spectra of cinnabar (red) and degraded cinnabar, identified as metacinnabar (black). **b,** Reference Raman spectra of cinnabar (red) and metacinnabar (black).[11,12] In both images, the position of the main peak is highlighted.

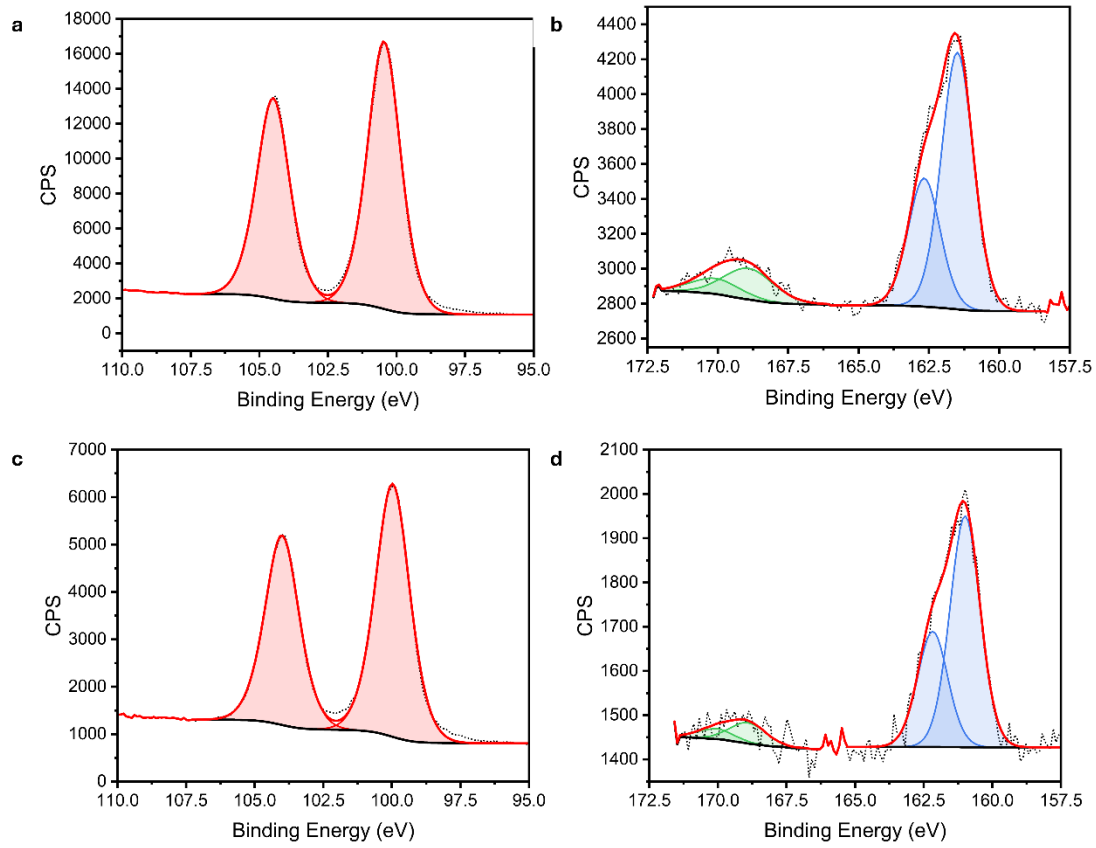


**Figure S12. a, c,** Hg 4f region of unaged cinnabar mock-ups and degraded cinnabar mock-ups respectively. **b,d,** S 2p region of unaged cinnabar mock-ups and degraded cinnabar mock-ups respectively. $S^{2-}$-related peaks have been fitted in blue, while $SO_4^{2-}$-related peaks in green.

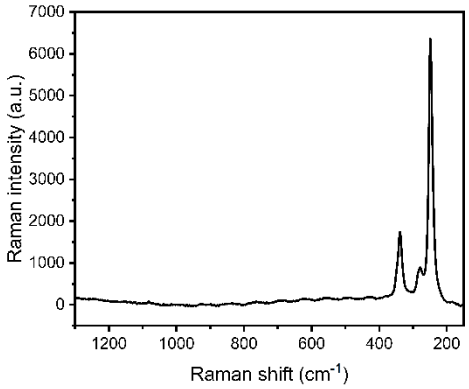


**Figure S13.** Raman spectrum of cinnabar identified on real frescoes fragments from the archaeological site of Aquileia.

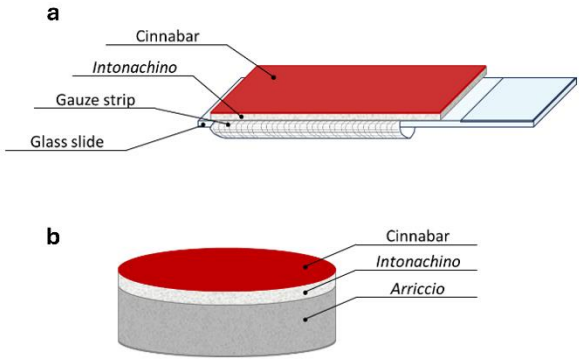


**Figure S14.** Schematic representation of the fresco mock-ups employed in this study. **a,** Simplified mock-up comprising *intonachino* and pigments. **b,** Complete mock-up with *arriccio*, *intonachino,* and pigment.

**Table S1.** Average viscosity of the prepared chitosan formulations.

| Sample | Viscosity [mPa*s] |
|---|---|
| *cs02* | $1.54*10^2$ |
| *cs04* | $1.54*10^3$ |
| *cs1* | $2.08*10^3$ |
| *cs2* | $4.75*10^4$ |

**Table S2.** Microscopic images of fresco mock-ups before and after the application of the coating, correlated with the respective ΔE values.

| | *cs02* | *cs04* | *cs1* | *cs2* |
|---|---|---|---|---|
| **Uncoated** | 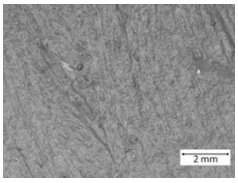 | 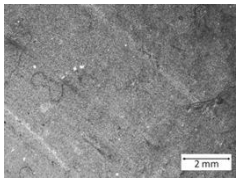 | 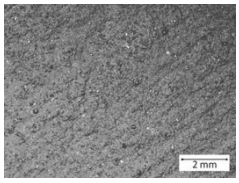 | 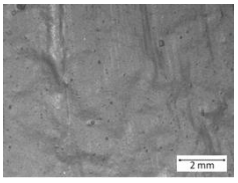 |
| **Coated** | 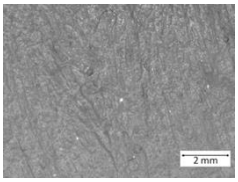 | 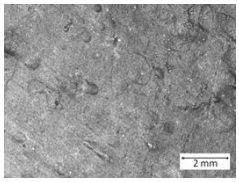 | 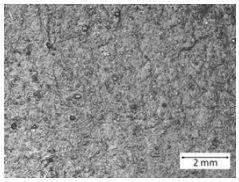 | 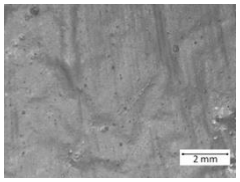 |
| **ΔE** | 1 | 2 | 1 | 2 |

**Table S3.** Average water surface contact angle of the 4 coating formulations applied on fresco mock-ups and representative images.

| Sample | Contact angle [°] | |
|---|---|---|
| *cs02* | 42.8 | 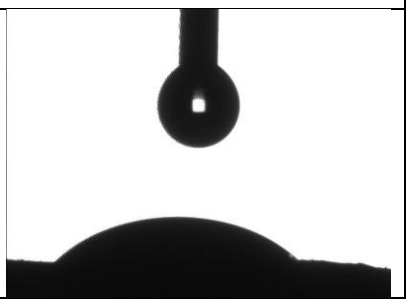 |

| | | |
|---|---|---|
| *cs04* | 45.2 | 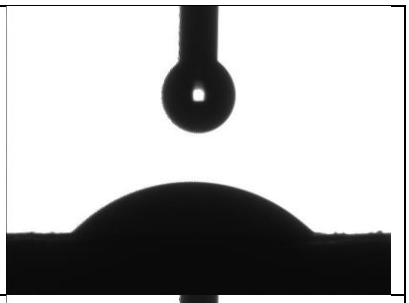 |
| *cs1* | 48.7 |  |
| *cs2* | 51.2 | 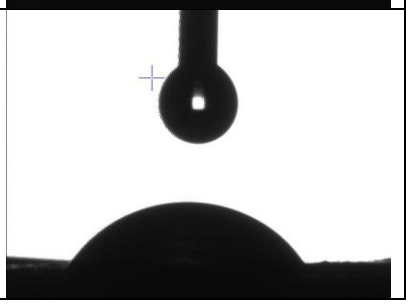 |

**Table S4.** Results from the colorimetric analysis performed on coated and uncoated fresco mock-ups at different degradation stages. All measurements were achieved as average of two points on opposites sides of the surface ofeach mock-up to account for the hetereogenity of the samples.

| | **8 hours** | **16 hours** | **24 hours** | **48 hours** | **72 hours** |
|---|---|---|---|---|---|
| *Uncoated* | 7.4 ± 0.8 | 12.3 ± 1.4 | 13.7 ± 0.1 | 25.7 ± 8.3 | 29.8 ± 10.1 |
| *cs04* | 1.9 ± 0.6 | 3.6 ± 0.4 | 7.1 ± 0.4 | 10.2 ± 0.4 | 12.12 ± 0.03 |
| *cs04-NPs* | 1.7 ± 1.2 | 1.9 ± 0.7 | 3.9 ± 0.8 | 5.2 ± 0.2 | 7.6 ± 0.4 |
| *cs1* | 4.2 ± 0.4 | 6.6 ± 1.3 | 7.3 ± 1.2 | 10.2 ± 1.3 | 13.3 ± 2.1 |
| *cs1-NPs* | 4.5 ± 0.9 | 3.2 ± 0.5 | 2.7 ± 0.6 | 4.3 ± 0.3 | 6.4 ± 0.2 |

**Table S5.** Pictures of the uncoated and coated fresco mock-ups at different degradation stages. The pictures represent the effect of the exposure of frescoes to UV light, chlorine-based salts, and high relative humidity.

| | **0 hours** | **8 hours** | **16 hours** | **24 hours** | **48 hours** | **72 hours** |
|---|---|---|---|---|---|---|

| | | | | | | |
|---|---|---|---|---|---|---|
| *Uncoated* |  |  |  |  |  |  |
| *cs04* |  |  |  |  |  |  |
| *cs04-NPs* |  |  |  |  |  |  |
| *cs1* |  |  |  |  |  |  |
| *cs1-NPs* |  |  |  |  |  |  |

REFERENCES


1 M. Radepont, Y. Coquinot, K. Janssens, J.-J. Ezrati, W. de Nolf and M. Cotte, *J. Anal. At. Spectrom.*, 2015, **30**, 599–612.
2 J. Yu, W. S. Warren and M. C. Fischer, *Sci. Adv.*, 2019, **5**, eaaw3136.
3 E. Gliozzo, *Archaeol. Anthropol. Sci.*, 2021, **13**, 210.
4 W. Anaf, K. Janssens and K. De Wael, *Angew. Chem.*, 2013, **125**, 12800–12803.
5 K. Elert, M. Pérez Mendoza and C. Cardell, *Commun. Chem.*, 2021, **4**, 1–10.
6 R. Nöller, *Stud. Conserv.*, 2015, **60**, 79–87.
7 K. Keune and J. J. Boon, *Anal. Chem.*, 2005, **77**, 4742–4750.
8 S. Pérez-Diez, A. Pitarch Martí, A. Giakoumaki, N. Prieto-Taboada, S. Fdez-Ortiz de Vallejuelo, A. Martellone, B. De Nigris, M. Osanna, J. M. Madariaga and M. Maguregui, *Anal. Chem.*, 2021, **93**, 15870–15877.
9 M. K. Neiman, M. Balonis and I. Kakoulli, *Appl. Phys. A*, 2015, **121**, 915–938.
10 M. Radepont, W. de Nolf, K. Janssens, G. V. der Snickt, Y. Coquinot, L. Klaassen and M. Cotte, *J. Anal. At. Spectrom.*, 2011, **26**, 959–968.
11 Cinnabar R070532 - RRUFF Database: Raman, X-ray, Infrared, and Chemistry, https://rruff.info/cinnabar/display=default/R070532, (accessed December 4, 2024).
12 Metacinnabar R060950 - RRUFF Database: Raman, X-ray, Infrared, and Chemistry, https://rruff.info/metacinnabar/display=default/R060950, (accessed December 4, 2024).
13 F. S. Gard, D. M. Santos, M. B. Daizo, E. Freire, M. Reinoso and E. B. Halac, *Appl. Phys. A*, 2020, **126**, 218.